Supporting Information

Origin of the Enhanced Photoluminescence Quantum Yield in $MAPbBr_3$ Perovskite with Reduced Crystal Size

Nikolaos Droseros, [◊,‡] Giulia Longo, [#] Jan C. Brauer, [‡] Michele Sessolo, [#] Henk J. Bolink, [#] Natalie Banerji [◊,‡*]

[◊]Department of Chemistry and Biochemistry, University of Bern, Freiestrasse 3, CH-3012 Bern, Switzerland

[‡]Department of Chemistry, University of Fribourg, Chemin du Musée 9, CH-1700 Fribourg, Switzerland

[#]Instituto de Ciencia Molecular, Universidad de Valencia, Catedràtico José Beltràn 2, 46980 Paterna, Spain

Corresponding Author

* natalie.banerji@dcb.unibe.ch

1. Experimental details:

1.1 Sample preparation: Methylammonium bromide (MABr), lead bromide ($PbBr_2$), polyvynilpirrolidone (PVP) and 9,9-spirobifluoren-2-yl-diphenyl-phosphine oxide (SPPO1) were used as received without further purification. The $MAPbBr_3$ precursor solution was prepared by dissolution of MABr and $PbBr_2$, in a molar ratio 3:1, in dimethylformamide (DMF) with a total concentration of 100 mg/mL. For the microcrystal and nanocrystal precursor solutions, 20 wt% of PVP and 50 wt% of SPPO1 were added to the solution. The samples analyzed in this work were prepared by single step spin coating of the corresponding solution at 2000 rpm for 60 seconds on glass substrates. All films were annealed at 90 ºC for 15 minutes. All processes described were carried out in a nitrogen-filled glovebox.

1.2 Steady state spectroscopy: The steady state photoluminescence spectra were recorded with an Edinburgh Instruments FS5 spectrofluorometer. The steady state absorption spectra were recorded with a Perkin Elmer UV/VIS/NIR Lambda 900 Spectrometer, equipped with a 150 mm integrating sphere.

1.3 Nanosecond-resolved photoluminescence (PL) and transient absorption (TA) spectroscopy: Both the time-resolved PL and the ns-TA measurements were performed with 450 nm pulsed excitation. The excitation pulses were generated by the fundamental near-UV pulses of a Q-switched Surelite Continuum Laser (3 ns, 355 nm, 10 Hz) and frequency converted in an Optical Parametrical Oscillator (GWU Versa scan). For the detection, an Andor i-Star camera, coupled to a monochromator, was used. For the ns-TA measurements, a flash lamp was used in order to generate a white light probe beam, which was overlapped with the pump beam on the sample, while the camera detected the variation of its transmission through the sample. The time-dependent emission/absorption of the excited state was obtained by varying the time-delay between the laser Q-switching and the camera detection time.

1.4 Femtosecond-resolved TA spectroscopy: Transient absorption measurements were performed under 450 nm pulsed excitation. The excitation pulses were generated from the fundamental near-infrared pulses of an amplified Ti:sapphire laser system (35 fs, 800 nm, 1 kHz, 6 mJ, Astrella Coherent) and frequency-converted by an optical

parametric amplifier (OPA, Opera Solo, Coherent). Broadband white light probe pulses covering the visible region from 450 nm to 770 nm were generated in a sapphire plate using part of the fundamental beam. The white light was split into two components that served as the signal and reference pulses. The probe pulses were temporally delayed relative to the excitation pulses via a micrometer translation stage, and pump-probe delays up to 2 ns were measured. Pump pulses of ~ 1 mm diameter photo-excited the sample (chopped at half the laser frequency), while the weaker probe pulses of ~ 250 μm diameter were used to probe the changes induced by pump excitation at different pump-probe delays. The different pump and probe beam diameters ensured a uniform distribution of detected photo-excited species. The signal probe pulses transmitted through the sample and the reference probe pulses were spectrally dispersed in a home-build prism spectrograph assembled by Entwicklungsbüro Stresing, Berlin and detected separately, shot-to-shot, by a pair of charge-coupled devices (CCD detectors, Hamamatsu S07030-0906).

1.5 Experimental conditions during the photophysical characterization: All the photophysical characterization described in SI sections 1.2 – 1.4 took place in a nitrogen filled, sealed chamber. In order to avoid exposure of the samples to atmospheric air, the transfer of the samples in the chamber took place inside the glovebox and the chamber was sealed before exiting the glovebox. The front and backside of the chamber are composed by two glass windows allowing the transmission of light. The excitation energy at each of the used wavelengths was adjusted after taking into account the reflectivity of the glass windows.

2. Crystal size and morphology of the polycrystalline film, the microcrystals and the nanocrystals

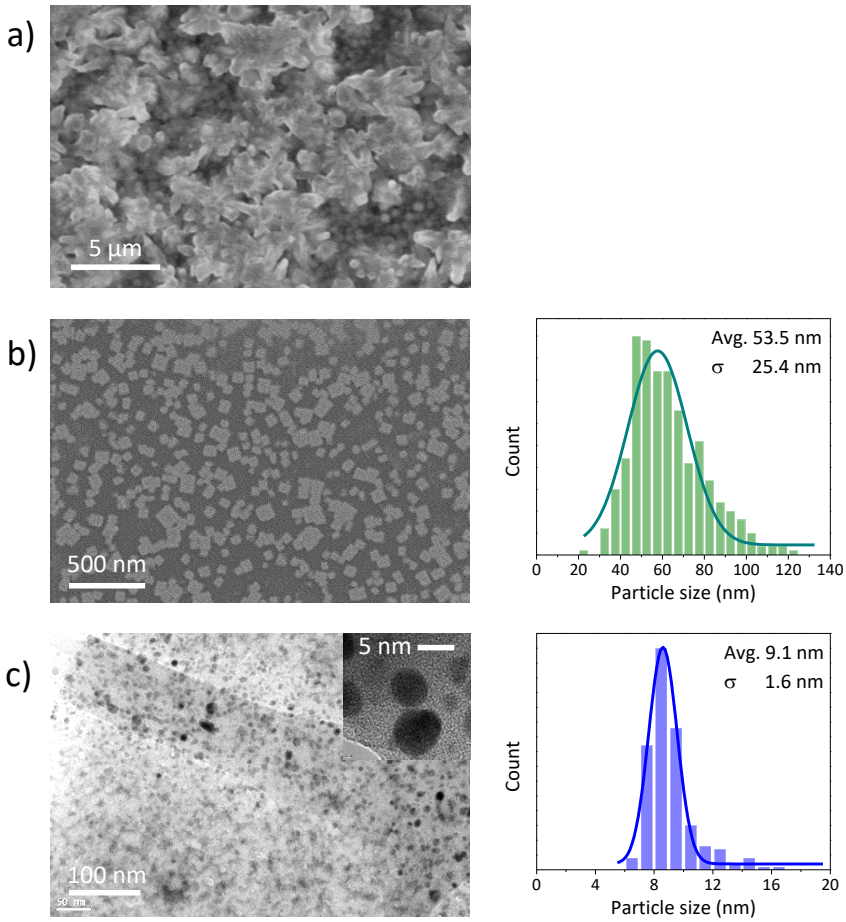

Figure S1: (a) SEM image of a polycrystalline $MAPbBr_3$ film and (b) a $MAPbBr_3$:PVP (microcrystalline) film. (c) TEM image of a scratched $MAPbBr_3$:SPPO1 sample highlighting the presence of nanocrystals (NCs, the inset shows a high magnification TEM image of the sample). On the right side, the particle size distributions estimated from the SEM and TEM images are reported, including their Gaussian fit, the average values and the standard deviation.

3. Calculation of the excitation densities

The excitation density was calculated by using the following equation:

$$n = (100 - T)\% \cdot \frac{E_{exc}}{h\nu \cdot \pi \cdot r^2 \cdot d} \cdot x \qquad (S1)$$

where T is the transmittance, E_{exc} the excitation energy per pulse, h the Planck's constant, v the excitation frequency, r the radius of the laser beam, d the thickness of the film and x is the volume ratio of the perovskite and the additive reported in Table S1. The film thickness was measured by a surface profilometer and the values are also shown in Table S1. The volume ratio, x, is added in the equation in order to take into account that the laser beam at the excitation wavelength of 450 nm was absorbed only by the perovskite and not by the additive contained in the film.

The calculation of this parameter x was performed in the following way: The weight ratio of the perovskite and the additive is known from the synthetic procedure that was followed, then this weight ratio can be transformed into molar ratio, by using the molecular weight of the components. Next, by using the volume of the perovskite unit cell and the one of the additive molecules, the volume of each material can be calculated. The volume of the unit cell of the $CH_3NH_3PbBr_3$ and its density were taken from Zhao et al.,[1] according to which they are 209.17 $Å^3$ and 4.92134 gr/cm^3, respectively. The molecular weight of PVP is $M_{r,PVP}$=111.1 gr/mol and its density is d_{PVP}= 1.2 gr/cm^3. The molecular weight of SPPO1 is $M_{r,SPPO1}$=516.57 gr/mol. Supposing that the total weight of both the perovskite precursor and additive used to prepare the solution is w and that x_{wt} is the weight percentage (wt%) of the additive, then it follows that in $x_{wt} \cdot w$ milligrams of the mixture there are $(x_{wt} \cdot w)/M_w$ moles of the additive. The quantities calculated in this way refer to the whole solution, but it can be safely assumed that the ratio between the two materials will be the same in the thin film cast from the solution. The weight percentage of each substance contained in the solutions is known. The volume of PVP can be calculated since its density is known. For the SPPO1, the volume of one molecule was calculated with the software Spartan (V_{SPPO1}= 542.02·10^{-24} cm^3) Finally, the total SPPO1 volume was calculated by the equation $V_{tot}=V_{SPPO1} \cdot n \cdot N_A$, where n is the number of moles of SPPO1 and N_A is Avogadro's number.

Table S1: Table showing the thickness of the films, the weight percentage of the perovskite and the additive, and their volume ratio in the thin films

Sample	Film thickness (nm)	w/w content of each material	Volume ratio between the additive and the perovskite
Polycrystalline perovskite	**70**	**100% $MAPbBr_3$**	_
Microcrystals	**65**	**20% PVP: 80% $MAPbBr_3$**	1.02
Nanocrystals	**110**	**50% SPPO1: 50% $MAPbBr_3$**	3.11

4. Time-Integrated PL spectra for the polycrystalline perovskite, the microcrystals and the nanocrystals

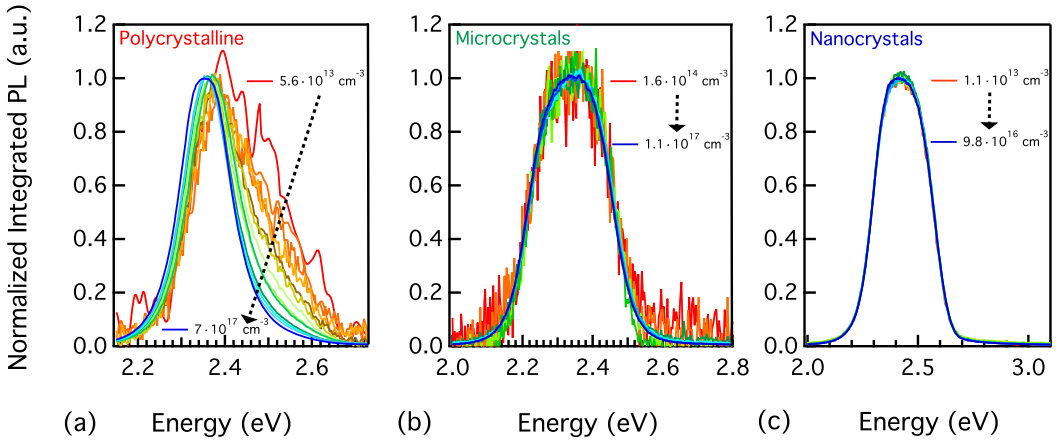

Figure S2: Time-integrated PL spectra for (a) the polycrystalline perovskite, (b) the microcrystals and (c) the nanocrystals. By increasing the excitation density, the PL spectra of the polycrystalline perovskite red shift and become narrower, while the integrated PL of the microcrystals and the nanocrystals shows no spectral change. All spectra are normalized to the value of the maximum PL intensity.

5. PL_0 vs. fluence (excitation density)

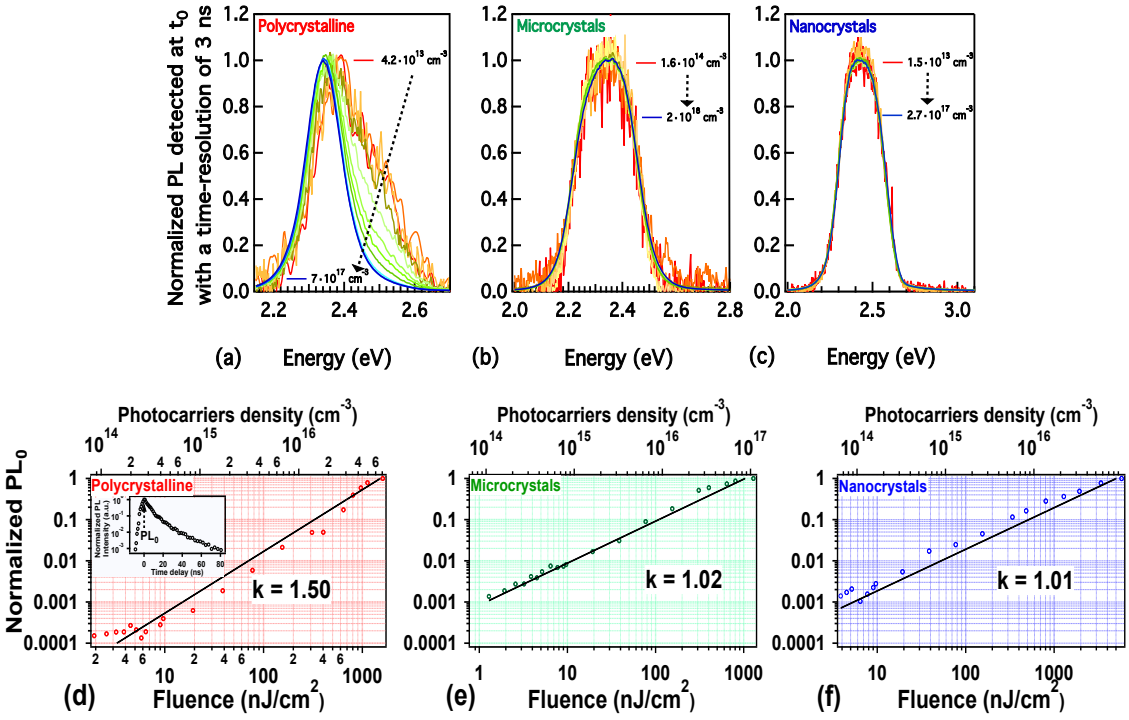

Figure S3: (a)-(c) Graphs showing the PL spectra detected at t_0 of the TRPL measurements with a time-resolution of 3 ns for (a) the polycrystalline perovskite, (b) the microcrystals and (c) the nanocrystals. These data were recorded directly after the equivalent time-integrated PL measurements shown in Fig. S2, on the same sample spot. **(d)-(f)** Graphs showing the fluence (excitation density) dependence of PL_0 detected at t_0 of the TRPL measurements (as shown in the inset of panel (d)) for (d) the polycrystalline perovskite, (e) the microcrystals and (f) the nanocrystals. On each graph, the fitting of the data with a power law function, $PL_0 \sim F^k$, is shown.

Comment on sample stability and data reversibility: The spectra shown in Fig. S4 (a)-(c) at t_0 were recorded using the same samples as the ones reported in the main text and the measurements were performed directly after the time-integrated PL measurements shown in Fig. S2 on the same excitation spot. Exactly the same spectral features, such as the red-shift of the maximum PL peak and the reduction of the intensity of the high energy part with increasing excitation density, are seen as for the previous time-integrated PL measurements. Apart from showing that the emission properties are already determined at t_0 = 3 ns, this also evidences that the samples were not degraded after the exposure to high excitation densities during the time-integrated PL measurements, and that the processes were reversible since they were observed again when repeating the experiment. The observed spectral changes when increasing the fluence can thus safely be assigned to the conversion of free carriers into excitons as reported in the main text. For an additional evidence of the photo-stability of the samples, see section 6 and Fig. S4 below.

6. Photo-stability study (under white light illumination)

As mentioned in refs. 71 and 72 of the main text, the change in the TRPL dynamics with increasing excitation density could originate from a photo-induced formation of traps or from ion migration taking place at high excitation densities. To confirm the photo-stability of our samples during the TRPL measurements and to exclude the effects of ref. 71 and 72, we have measured the TRPL dynamics for two samples at a common carrier density, once with an additional illumination provided by a continuous white light source and once without. These measurements were performed on the same samples reported in the main text, after the time-integrated PL, the PL at t_0 and the TRPL measurements. Fig. S4 shows the results for the polycrystalline perovskite and the microcrystals.

As shown in Fig. S4, the dynamics are the same and are not affected by the additional illumination provided by the white light source. Furthermore, the dynamics are the same as the ones reported at the high excitation density in the main text (i.e. they are reproducible). If the formation of more traps had been induced by the white light illumination, different decay dynamics would have been

expected, but this is not the case here. Thus, these measurements support both the assignment of the spectral changes during the integrated PL measurements to the conversion of free carriers to excitons, and the assignment of the initial slow-down of the TRPL dynamics with increasing fluence to trap filling.

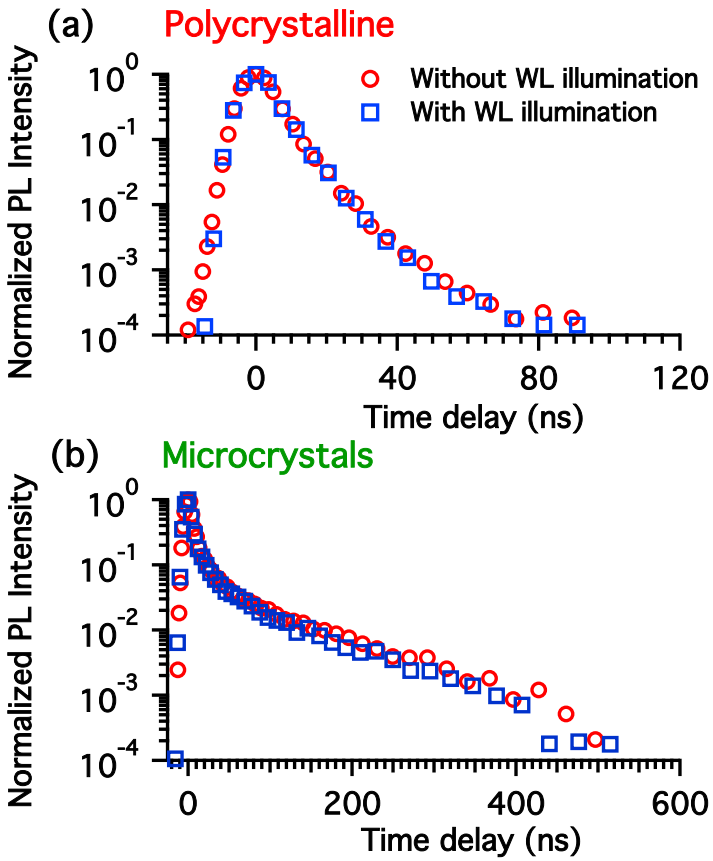

Figure S4: TRPL dynamics recorded under 355 nm excitation, with (blue squares) and without (red circles) continuous white light (WL) illumination for (a) the polycrystalline perovskite (excitation density of $3 \cdot 10^{17}$ cm^{-3}) and (b) the microcrystals (excitation density of $4 \cdot 10^{17}$ cm^{-3}).

7. Time-Integrated PL spectra of the neat perovskite analyzed with a double Gaussian function

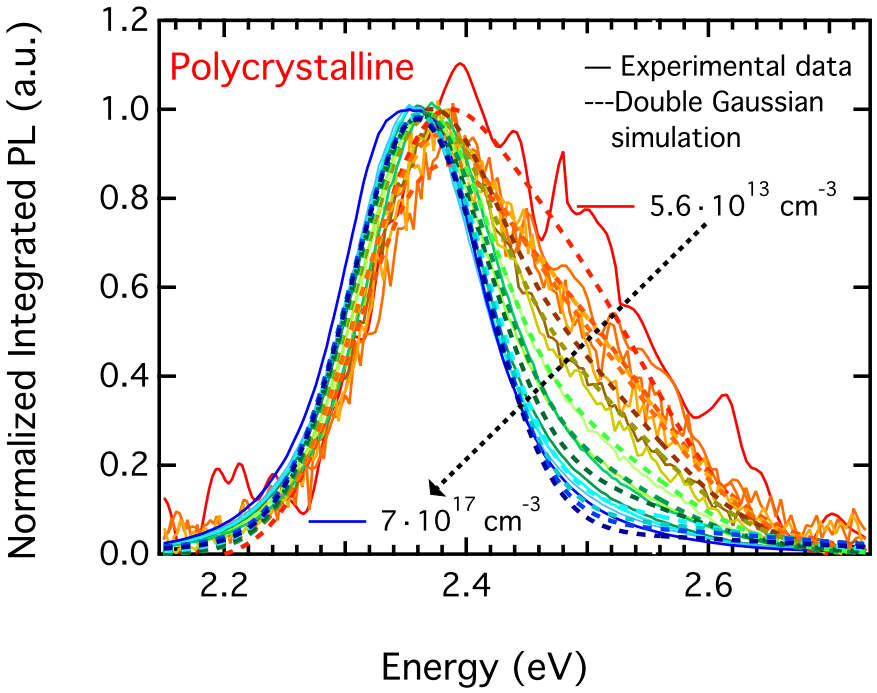

Figure S5: Time-integrated PL spectra of the polycrystalline perovskite at various excitation densities. On the same graph, the simulation with a double Gaussian function for each excitation density is shown. All the spectra are normalized to the value of the maximum PL intensity.

8. Calculation of the error bars for the Saha model

The error bars in the graph of the ratio of free carriers over excitons at different excitation densities (main text Figure 2(d)) were obtained by inserting the experimental uncertainties in the Saha equation. The use of the error propagation theory resulted to the following equations for the error calculation:

$$\delta n = |n|\sqrt{\left(\frac{\delta E_{exc}}{E_{exc}}\right)^2 + \left(\frac{\delta r^2}{r^2}\right)^2} \quad \text{(S2)}$$

where E_{exc} is the energy per pulse and r the radius of the laser beam.

$$\delta \mu^* = |\mu^*|\sqrt{\left(\frac{\delta b^*}{b^*}\right)^2} \quad \text{(S3)}$$

with μ^* being the reduced effective mass of the exciton and b standing for the slope of the eq. 2 (main text).

$$\delta R = |R|\sqrt{\left(\frac{\delta n}{n}\right)^2 + \left(\frac{3}{2}\frac{\delta \mu}{\mu}\right)^2 + \left(\frac{3}{2}\frac{\delta T}{T}\right)^2 + \left(\frac{\delta E_b}{E_b}\right)^2} \quad \text{(S4)}$$

where R stands for the ratio between the squared population of the free carriers over the population of the excitons from eq. 3 (main text), and T is the temperature. The resulting errors are reported in Tables S2 and S3 below.

Table S2: Values and errors for the excitation density independent magnitudes

Magnitude symbol	Value	Error symbol	Error value
b	$8.38 \cdot 10^{-13}$ (eV/cm^2)	**δb**	$6.18 \cdot 10^{-14}$ (eV/cm^2)
b^*= b/m_o	1475.4 (J/m^2)	**δb***	108.8 (J/m^2)
μ (in m_o)	0.051 m_o	**δμ**	0.012 m_o
T	294.15 (K)	**δT**	0.5 (K)
r	0.004 (m)	**δr**	0.0005 (m)
r^2	0.000016 (m^2)	**δr^2**	0.000016 (m^2)
E_b	0.11 (eV)	**δE_b**	0.01 (eV)

Table S3: Values of all the parameters that depend on the excitation density along with their errors

Excitation Energy (nJ)	δE (nJ)	n (cm^{-3})	δn	R (FC/Exc)	δR
0.8	0.08	$5.66 \cdot 10^{13}$	$1.52 \cdot 10^{13}$	0.98	0.46
1.2	0.12	$8.50 \cdot 10^{13}$	$2.28 \cdot 10^{13}$	0.97	0.45
1.6	0.16	$1.13 \cdot 10^{14}$	$3.05 \cdot 10^{13}$	0.96	0.45
2	0.2	$1.42 \cdot 10^{14}$	$3.81 \cdot 10^{13}$	0.95	0.44
2.4	0.24	$1.70 \cdot 10^{14}$	$4.57 \cdot 10^{13}$	0.94	0.44
2.8	0.28	$1.98 \cdot 10^{14}$	$5.33 \cdot 10^{13}$	0.93	0.43
3.2	0.32	$2.27 \cdot 10^{14}$	$6.10 \cdot 10^{13}$	0.93	0.43
3.6	0.36	$2.55 \cdot 10^{14}$	$6.86 \cdot 10^{13}$	0.92	0.43
4	0.4	$2.83 \cdot 10^{14}$	$7.62 \cdot 10^{13}$	0.91	0.42
4.8	0.48	$3.40 \cdot 10^{14}$	$9.15 \cdot 10^{13}$	0.9	0.42
5.6	0.56	$3.96 \cdot 10^{14}$	$1.06 \cdot 10^{14}$	0.89	0.42
6	0.6	$4.25 \cdot 10^{14}$	$1.14 \cdot 10^{14}$	0.87	0.41
12	1.2	$8.50 \cdot 10^{14}$	$2.28 \cdot 10^{14}$	0.8	0.38
24	2.4	$1.70 \cdot 10^{15}$	$4.57 \cdot 10^{14}$	0.69	0.32
48	4.8	$3.40 \cdot 10^{15}$	$9.15 \cdot 10^{14}$	0.57	0.27
96	9.6	$6.80 \cdot 10^{15}$	$1.83 \cdot 10^{15}$	0.46	0.21
192	19.2	$1.36 \cdot 10^{16}$	$3.66 \cdot 10^{15}$	0.35	0.16
250	25	$1.77 \cdot 10^{16}$	$4.76 \cdot 10^{15}$	0.32	0.15
400	40	$2.83 \cdot 10^{16}$	$7.62 \cdot 10^{15}$	0.26	0.12
500	50	$3.54 \cdot 10^{16}$	$9.53 \cdot 10^{15}$	0.24	0.11
600	60	$4.25 \cdot 10^{16}$	$1.14 \cdot 10^{16}$	0.22	0.10
700	70	$4.96 \cdot 10^{16}$	$1.33 \cdot 10^{16}$	0.2	0.09
800	80	$5.66 \cdot 10^{16}$	$1.52 \cdot 10^{16}$	0.19	0.08
900	90	$6.37 \cdot 10^{16}$	$1.71 \cdot 10^{16}$	0.18	0.08
1000	100	$7.08 \cdot 10^{16}$	$1.90 \cdot 10^{16}$	0.17	0.08
1200	120	$8.50 \cdot 10^{16}$	$2.28 \cdot 10^{16}$	0.16	0.07
1400	140	$9.91 \cdot 10^{16}$	$2.66 \cdot 10^{16}$	0.15	0.07
1800	180	$1.27 \cdot 10^{17}$	$3.43 \cdot 10^{16}$	0.135	0.06
3600	360	$2.55 \cdot 10^{17}$	$6.86 \cdot 10^{16}$	0.095	0.04
7200	720	$5.10 \cdot 10^{17}$	$1.37 \cdot 10^{17}$	0.065	0.03

9. Population rates from TRPL, ns-TA and fs-TA measurements

These graphs show the rate of the population returning to the ground state under different excitation densities. The PL was detected at the PL maximum, while for the TA measurements the ground state bleaching (GSB) band was probed. To be able to analyze the results with the polynomial equations provided above, the data obtained under ns excitation had to be shifted to match the ones obtained under fs excitation by a value corresponding to the carrier generation term. The equation 4 in the main text includes a carrier generation rate term, G_0 in the population rate of the excited state. In the case that temporally very short excitation pulses induce the excitation, the generation term can be set to zero. This is valid in the case of the fs-TA measurements, but not for the measurements obtained under excitation with ns pulses. In this case, the generation term has to be included. The presence of temporally longer generation of carriers in the ns-TA and TRPL measurements causes the offset in (black arrow in Figure S5).

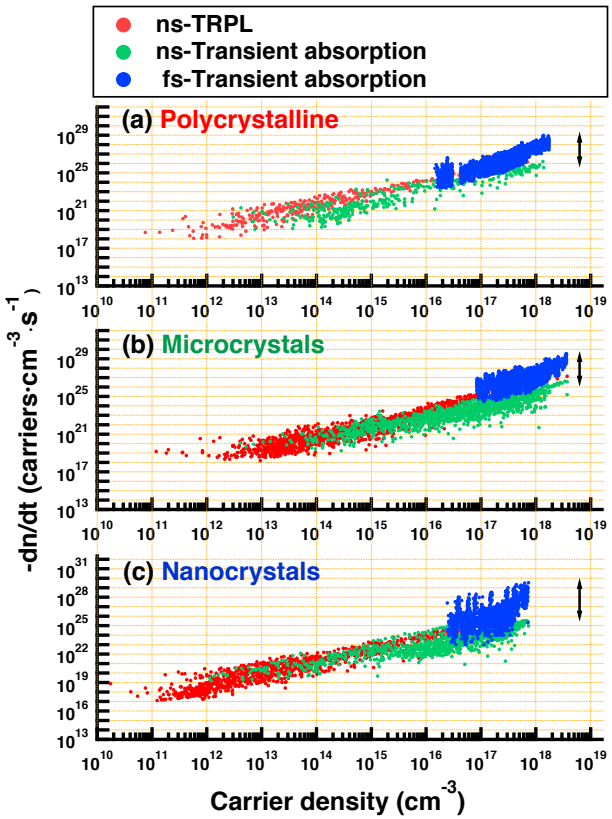

Figure S6: Population rate vs. carrier density for (a) the polycrystalline perovskite, (b) the microcrystals and (c) the nanocrystals. The data derived from ns-TRPL, ns-TA and fs-TA measurements are denoted with a different color. The black arrows denote the offset induced by the inclusion of a carrier generation term in the measurements performed under excitation with ns pulses.

REFERENCES

(1) Zhao, P.; Xu, J.; Dong, X.; Wang, L.; Ren, W.; Bian, L.; Chang, A. Large-Size CH3NH3PbBr3 Single Crystal: Growth and in Situ Characterization of the Photophysics Properties. *J. Phys. Chem. Lett.* **2015**, *6* (13), 2622–2628.